symmetry

MDPI

*Article*

# The Shadows of Regular Black Holes with Asymptotic Minkowski Cores

**Yi Ling [1,2] and Meng-He Wu [3,4,*]**

1 Institute of High Energy Physics, Chinese Academy of Sciences, Beijing 100049, China
2 School of Physics, University of Chinese Academy of Sciences, Beijing 100049, China
3 School of Mathematics, Physics and Statistics, Shanghai University of Engineering Science, Shanghai 201620, China
4 Center of Application and Research of Computational Physics, Shanghai University of Engineering Science, Shanghai 201620, China
* Correspondence: mhwu@sues.edu.cn

**Abstract:** We investigate the shadows cast by a sort of new regular black hole which are characterized by an asymptotic Minkowski core and sub-Planckian curvature. First, we extend the metric with spherical symmetry to the one of rotating Kerr-like black holes and derive the null geodesics with a circular orbit near the horizon of the black hole. Then, we plot the shadows of black holes with different values for the deviation parameter. It is found that the size of the shadow shrinks with the increase in the deviation parameter, while the shape of the shadow becomes more deformed. In particular, by comparing with the shadow a Bardeen black hole and Hayward black hole with the same parameter values, we find that, in general, the shadows of black holes with Minkowski cores have larger deformations than those with de Sitter cores, which potentially provides a strategy to distinguish these two sorts of regular black holes with different cores by astronomical observation in the future.

**Keywords:** regular black hole; black hole shadow; shadow cast



**Citation:** Ling, Y.; Wu, M.-H. The Shadows of Regular Black Holes with Asymptotic Minkowski Cores. *Symmetry* **2022**, *14*, 2415. https://doi.org/10.3390/sym14112415

Academic Editors: Gonzalo J. Olmo, Adrián Del Río Vega and Eduardo J. Sánchez Villaseñor

Received: 22 October 2022
Accepted: 10 November 2022
Published: 15 November 2022



## 1. Introduction

The release of the first photo of black hole shadows by the Event Horizon Telescope (ETH) cooperation team announced the coming of a new age for measuring the nature of astrophysical black holes [1,2]. Just recently, the ETH collaboration released a photo of the supermassive black hole Sgr A*, which provides overwhelming evidence for the existence of a black hole at the center of the Milky Way [3,4]. Now, it is fair to say that more and more astronomical evidence has been making it possible for people to justify various theoretical thoughts on black holes through the experimental observation of black hole shadows. As a matter of fact, the shadows of different black holes were previously explored theoretically in [5–11], and a recent review on this topic can be found in [12]. For instance, the shadow of a Schwarzschild black hole was first studied by Synge in [5] and Luminet in [6]. Unsurprisingly, they found that its shadow was a perfect circle. A little bit later, the shadow of the Kerr black hole was studied in [7,8]. Its shadow is no longer circular but has a deformation in the direction of rotation, which provides an abundant structure for the shadow of black holes, and in principle, one may obtain the nature of rotating black holes by observing its shadow, such as the mass, spin and charge of black holes [13–17]. By virtue of black hole shadows, some fundamental problems on the nature of gravity have also been explored, such as modified gravity, the candidates for dark matter and the quantum effect of gravity, among others [18–29].

Recently, investigation of the shadows has been extended to regular black holes as well, including rotating Bardeen and Hayward black holes [30–33]. In history, regular black holes are proposed to resolve the singularity problem in classical general relativity. Taking the quantum effects of gravity into account, it is believed that these singularities could be removed or avoided. Before a well-defined theory of quantum gravity could be established, people constructed various regular black holes without singularity at the phenomenological level [34–40]. These regular black hole models are characterized by a finite Kretschmann scalar curvature. Currently, as far as we know, there exist various ways to classify regular black holes either by their symmetry [41,42] or by their asymptotic behavior near the center of the black hole. In this paper, we classify regular black holes into two classes according to the latter. One is the regular black holes with asymptotic de Sitter cores, such as Bardeen black holes, Hayward black holes as well as Frolov black holes. The other one is regular black holes with asymptotic Minkowski cores, which are characterized by an exponentially suppressing Newton potential.

Our current work is motivated to answer the following question: How does one diagnose a detected black hole to be an ordinary black hole with singularity rather than a regular black hole without singularity? Without a doubt, this is a very crucial issue in the nature of detecting black holes and has a significant impact on the theory of gravity. Unfortunately, since the singularity hides inside the horizon, it is currently impractical to distinguish these two kinds of black holes by diving into the black hole or detecting any signal coming out from the interior of the horizon. Nevertheless, with the accumulation of the observation data on detected black holes, we wonder if one can distinguish a regular black hole from a traditional black hole with singularity by observing the shadows of black holes. Therefore, investigating the shadows of regular black holes theoretically, as performed in this manuscript, could shed light on this issue and improve our understanding of the observation data of detected black holes. Previously, the shadows of regular black holes with de Sitter cores were investigated in [30], and the study of shadows has also been extended to regular black holes with Minkowski cores [43–45]. However, the black holes with Minkowski cores previously studied in the literature have a shortcoming. From the viewpoint of quantum gravity, the Kretschmann scalar curvature of a regular black hole should be sub-Planckian everywhere and at any time, whereas the Kretschmann scalar curvature of the previously discussed black hole with a Minkowski core is mass-dependent such that its Kretschmann scalar curvature could easily exceed the Planck mass density by increasing the mass of the black hole. This implies that the regular black holes with Minkowski cores previously used to study black hole shadows only make sense for small masses at the Planck scale [39]. On the other hand, the Kretschmann scalar curvatures of Bardeen black holes and Hayward black holes which have de Sitter cores are mass-independent [39]. The scalar curvatures of these sorts of black holes exhibit distinct behavior. Thus, in the previous literature, no one could compare the shadows of these two sorts of black holes. In this paper, we intend to investigate the shadow of a regular black hole with a Minkowski core characterized by a mass-independent Kretschmann scalar curvature [39] and compare it with the shadow of one with the same parameter values but with a de Sitter core.

We organized this paper as follows. In the next section, we extend the regular black hole with spherical symmetry proposed in [39] to the rotating Kerr-like one and then obtain the null geodesics with a circular orbit near the horizon of a black hole with the Hamilton–Jacobi formalism. In Sections 3 and 4, we will investigate the shadows of regular black holes with $(\gamma = 2/3, n = 2)$ and $(\gamma = 1, n = 3)$, respectively, and compare them with the shadows of Bardeen and Hayward black holes with the same parameter values. Furthermore, we will compute the upper limit of the deviation from the circularity and compare our theoretical results with the observation data for the shadow of a supermassive black hole at the center of the galaxy (M87*) by the ETH. It is found that the shadows of regular black holes are highly compatible with the shadow observed by the ETH as well. Our conclusions and discussions are given in Section 5.

## 2. Rotating Kerr-like Regular Black Hole with a Minkowski Core

In [39], we proposed a new sort of regular spherically symmetric black hole with the following metric:

$$ds^2 = -f(r)dt^2 + f(r)^{-1}dr^2 + r^2(d\theta^2 + \sin^2\theta d\phi^2), \tag{1}$$

with

$$f(r) = 1 - \frac{2m(r)}{r}, \tag{2}$$

where $m(r)$ takes the form of

$$m(r) = Me^{-g^n M^\gamma / r^n}. \tag{3}$$

We set $G = 1$ throughout this paper. We remark that the above metric form can be understood as the solution of the Einstein field equation, in which the gravitational field is coupled to a nonlinear Maxwell field. The physical source of a regular black hole could be interpreted as a nonlinear electromagnetic field [46]. The generic form of the stress–energy tensor and a discussion on the violation of the strong energy condition is presented in [39].

This sort of regular black hole exhibits the following two prominent characteristics. First, the exponentially suppressing form of the Newton potential leads to a non-singular Minkowski core at the center of the black hole, which was originally proposed in [38], but with the specific form of $\gamma = 0, n = 2$. Secondly, under the condition $3/n < \gamma < n$, the Kretschmann scalar curvature can always be sub-Planckian regardless of the mass of the black hole once the parameter $g$ is appropriately fixed. Finally, the correspondence of such regular black holes to the ones with asymptotic de Sitter cores was pointed out in [39], where $m(r)$ took the form of

$$m(r) = \frac{Mr^{\frac{n}{\gamma}}}{(r^n + \gamma g^n M^\gamma)^{1/\gamma}}. \tag{4}$$

Specifically, $\gamma = 2/3, n = 2$ leads to a Bardeen black hole, while $\gamma = 1, n = 3$ leads to a Hayward black hole.

In this paper, in order to obtain a non-circular shadow with distortions, we extend the above metric with $m(r)$ given in Equation (3) to describe a rotating Kerr-like black hole. We employ the Newman–Janis algorithm [47–53] for a static, spherical regular black hole in Equation (1) and obtain a rotating regular black hole. For a spherical symmetric metric (Equation (1)), we introduce $du = dt - dr/f(r)$ to find the null coordinates $\{u, r, \theta, \phi\}$. The metric becomes

$$ds^2 = -f(r)du^2 - 2dudr + r^2\left(d\theta^2 + \sin^2\theta d\phi^2\right). \tag{5}$$

The inverse metric $g^{\mu\nu}$ can be represented by a null tetrad $\left(l^\mu, n^\mu, m^\mu, m^{\dagger\mu}\right)$ as

$$g^{\mu\nu} = -l^{\mu^\nu} n^v - l^v n^\mu + m^\mu m^{\dagger\nu} + m^v m^{\dagger\mu}, \tag{6}$$

with the relation

$$l_\mu l^\mu = n_\mu n^\mu = m_\mu m^\mu = l_\mu m^\mu = n_\mu m^\mu = 0,\ l_\mu n^\mu = -m_\mu m^{\dagger\mu} = -1. \tag{7}$$

Then, the null tetrad $\left(l^\mu, n^\mu, m^\mu, m^{\dagger\mu}\right)$ can be expressed as

$$l^\mu = \delta^\mu_r, \quad n^\mu = \delta^\mu_u - \frac{f(r)}{2}\delta^\mu_r, \quad m^\mu = \frac{1}{\sqrt{2r^2}}\left(\delta^\mu_\theta + \frac{i}{\sin\theta}\delta^\mu_\phi\right). \tag{8}$$

The following complex coordinate transformation

$$r' = r + ia\cos\theta, \quad u' = u - ia\cos\theta, \tag{9}$$

is used for the null tetrad $\left(l^{\mu}, n^{\mu}, m^{\mu}, m^{\dagger\mu}\right)$ to become

$$\begin{aligned} l'^{\mu} &= \delta^{\mu}_{r}, \quad n'^{\mu} = \delta^{\mu}_{u} - \frac{\tilde{f}(r)}{2}\delta^{\mu}_{r}, \\ m'^{\mu} &= \frac{1}{\sqrt{2(r' - ia\cos\theta)^2}}\left(ia\sin\theta\left(\delta^{\mu}_{u} - \delta^{\mu}_{r}\right) + \delta^{\mu}_{\theta} + \frac{i}{\sin\theta}\delta^{\mu}_{\phi}\right), \end{aligned} \tag{10}$$

with

$$\tilde{f}(r) = 1 - \frac{2m(r)r}{\Sigma}, \tag{11}$$

where $\Sigma = r^2 + a^2\cos^2\theta$ and $a$ is denoted as the spin parameter of an axisymmetric black hole. Using Equation (10), we can obtain a new inverse metric $g'^{\mu\nu}$ as follows:

$$g'^{\mu v} = -l'^{\mu}n'^{\nu} - l'^{\nu}n'^{\mu} + m'^{\mu}m'^{\dagger\nu} + m'^{\nu}m'^{\dagger\mu}, \tag{12}$$

whose explicit metric formula is

$$\begin{aligned} ds^2 = &-\tilde{f}(r)du^2 - 2dur' + 2a\sin^2\theta\left(\tilde{f}(r) - 1\right)dud\phi + 2a\sin^2\theta drd\phi \\ &+ \left(r' - ia\cos\theta\right)^2 d\theta^2 + \sin^2\theta\left[\left(r' - ia\cos\theta\right)^2 + a^2\sin^2\theta\left(2 - \tilde{f}(r)\right)\right]d\phi^2. \end{aligned} \tag{13}$$

Finally, we apply the following transformations to obtain the metric in Boyer–Lindquist coordinates:

$$du = dt' - \frac{\Sigma + a^2\sin^2\theta}{\Sigma f(r) + a^2\sin^2\theta}dr, \quad d\phi = d\phi' - \frac{a}{\Sigma f(r) + a^2\sin^2\theta}dr, \tag{14}$$

where $\Sigma = r^2 + a^2\cos^2\theta$. The new metric is given by

$$\begin{aligned} ds^2 = &-\tilde{f}(r)dt^2 + \frac{\Sigma}{\Sigma\tilde{f}(r) + a^2\sin^2\theta}dr^2 - 2a\sin^2\theta(1 - \tilde{f}(r))d\phi dt \\ &+ \Sigma d\theta^2 + \sin^2\theta\left[\Sigma - a^2(\tilde{f}(r) - 2)\sin^2\theta\right]d\phi^2. \end{aligned} \tag{15}$$

By substituting Equation (11) into Equation (15), we obtain a rotating regular black hole in Boyer– Lindquist coordinates:

$$\begin{aligned} ds^2 = &-\left(1 - \frac{2m(r)r}{\Sigma}\right)dt^2 - \frac{4am(r)r\sin^2\theta}{\Sigma}dtd\phi + \frac{\Sigma}{\Delta}dr^2 \\ &+ \Sigma d\theta^2 + \left(r^2 + a^2 + \frac{2a^2m(r)r\sin^2\theta}{\Sigma}\right)\sin^2\theta d\phi^2, \end{aligned} \tag{16}$$

with

$$\Delta = r^2 - 2m(r)r + a^2. \tag{17}$$

In this Kerr-like metric, $a$ is the rotation parameter, and obviously, as $a \to 0$, it returns to the metric given in Equation (1). Now, we plot the shadows of these sorts of black holes by closely following the route presented in [30], where the shadows of black holes with different mass functions $m(r)$ were investigated for Bardeen and Hayward black holes.

First, we consider the null geodesics near the horizon of the black hole. We start with a Lagrangian system for a photon

$$\mathcal{L} = \frac{1}{2}\left(\frac{ds}{d\sigma}\right)^2 = \frac{1}{2}g_{\mu\nu}\dot{x}^{\mu}\dot{x}^{\nu}, \tag{18}$$

where $\sigma$ is an affine parameter along the geodesics. Over a Kerr-like black hole background, $\partial/\partial t$ and $\partial/\partial \phi$ are killing vectors, and thus there are two conservative quantities corresponding to the energy and the angular momentum of the photon, respectively:

$$\begin{aligned} E &= -p_t = g_{tt}\dot{t}, \\ L_z &= p_\phi = g_{\phi\phi}\dot{\phi}. \end{aligned} \tag{19}$$

We can easily find

$$\begin{aligned} \Sigma\frac{dt}{d\sigma} &= a\left(L_z - aE\sin^2\theta\right) + \frac{r^2+a^2}{\Delta}\left[\left(r^2+a^2\right)E - aL_z\right], \\ \Sigma\frac{d\phi}{d\sigma} &= \left(\frac{L_z}{\sin^2\theta} - aE\right) + \frac{a}{\Delta}\left(\left(r^2+a^2\right)E - aL_z\right). \end{aligned} \tag{20}$$

The Hamilton–Jacobi equation for a null geodesic is given by

$$\frac{\partial S}{\partial \sigma} = -\mathcal{H}, \tag{21}$$

where $S$ is the Jacobi action and the Hamilton for a photon has the form

$$\mathcal{H} = p_\mu \dot{x^\mu} - \mathcal{L} = \frac{1}{2}g^{\mu\nu}p_\mu p_\nu = 0, \tag{22}$$

with $p_\mu \equiv \frac{\partial S}{\partial x^\mu}$ being the conjugate momentum of the photon. The system we consider is an integrable system, and thus the action can be expressed as

$$S = -Et + L_z\phi + S_r(r) + S_\theta(\theta). \tag{23}$$

By substituting Equations (16) and (23) into Equation (22), we obtain

$$\begin{aligned} &\left(\frac{dS_\theta}{d\theta}\right)^2 + \Delta\left(\frac{dS_r}{dr}\right)^2 - \left(\frac{1}{\Delta}\left(r^2+a^2\right)^2 - a^2\sin^2\theta\right)E^2 \\ &\quad + \frac{4am(r)r}{\Delta}EL + L^2\left(\frac{1}{\sin^2\theta} - \frac{a^2}{\Delta}\right) = 0. \end{aligned} \tag{24}$$

Due to the fact that coordinates $r$ and $\theta$ are separable, we can rewrite Equation (24) as

$$\begin{aligned} &\Delta\left(\frac{dS_r}{dr}\right)^2 - \frac{1}{\Delta}\left(r^2+a^2\right)^2E^2 + \frac{4arm(r)}{\Delta}EL - \frac{a^2}{\Delta}L^2 \\ &= -\left(\frac{dS_\theta}{d\theta}\right)^2 - a^2E^2\sin^2\theta - \frac{L^2}{\sin^2\theta} = \mathcal{K}, \end{aligned} \tag{25}$$

where $\mathcal{K}$ is the Carter constant. The relationship between $x^\mu$ and $p^\mu$ is

$$\frac{dx^\mu}{d\sigma} = p^\mu. \tag{26}$$

Thus, the geodesic equation of motion for $r$ and $\theta$ is given by

$$\begin{aligned} \Sigma\frac{dr}{d\sigma} &= \pm\sqrt{\mathcal{R}}, \\ \Sigma\frac{d\theta}{d\sigma} &= \pm\sqrt{\Theta}, \end{aligned} \tag{27}$$

with

$$\begin{aligned}\mathcal{R} &= \left[\left(r^2+a^2\right)E - aL_z\right]^2 - \Delta\left[\mathcal{K} + (L_z - aE)^2\right],\\ \Theta &= \mathcal{K} + \cos^2\theta\left(a^2E^2 - \frac{L_z^2}{\sin^2\theta}\right),\end{aligned} \tag{28}$$

The critical condition for unstable circular orbits is given by $\mathcal{R}(r) = 0$ and $d\mathcal{R}(r)/dr = 0$, and we introduce $\xi = L_z/E$ and $\eta = \mathcal{K}/E^2$ to determine unstable circular orbits. We can easily obtain the parameters $\xi$ and $\eta$ as follows:

$$\begin{aligned}\xi =& \frac{(a^2-3r^2)m + r(a^2+r^2)(1+m')}{a(m+r(-1+m'))},\\ \eta =& -\frac{r^3}{a^2}(r^3 + 9rm^2 + 2\left(2a^2r + r^3\right)m' + r^3m'^2\\ &- 2m(2a^2+3r^2+3r^2m'))(m+r(-1+m'))^{-2},\end{aligned} \tag{29}$$

where $m$ is the function of $r$ and the prime denotes the derivative with respect to the radius $r$.

Following [30], we introduce celestial coordinates $(\alpha, \beta)$ to visualize the black hole shadow:

$$\begin{aligned}\alpha &= \lim_{r_0\to\infty}\left(-r_0^2\sin\theta_0\frac{d\phi}{dr}\right),\\ \beta &= \lim_{r_0\to\infty}\left(r_0^2\frac{d\theta}{dr}\right),\end{aligned} \tag{30}$$

where $r_0$ is the distance between the black hole and the observer and $\theta_0$ is the inclination angle between the rotating axis of the black hole and the observer's line of sight. For the limit $r \to \infty$, the celestial coordinates have the following simple form:

$$\begin{aligned}\alpha &= -\xi\csc\theta_0,\\ \beta &= \pm\sqrt{\eta + a^2\cos^2\theta_0 - \xi^2\cot^2\theta_0}.\end{aligned} \tag{31}$$

## 3. Shadow of a Regular Black Hole with $\gamma = 2/3$ and $n = 2$

In this section, we study the shadow cast by a regular black hole with $\gamma = 2/3$ and $n = 2$, which exhibits the same asymptotical behavior as a Bardeen black hole at a large scale in the radial direction.

In Figure 1, we plotted the silhouettes of the shadows for various values of the rotation parameter $a/M$ and the deviation parameter $g/\left(\sqrt{\frac{3}{2}}M^{2/3}\right)$, which are understood to be dimensionless quantities. First, by comparing the left plot with the right one, we find that with the increase in the rotation parameter $a/M$, the left side of the silhouette of the shadow was more inclined to the vertical axis, which is similar to the phenomenon observed in [30]. Secondly, from both plots in Figure 1, we noticed that for the same rotation parameter $a/M$, the size of the shadow shrank with the increase in the deviation parameter $g/\left(\sqrt{\frac{3}{2}}M^{2/3}\right)$. Moreover, the silhouette of the shadow was more deformed for the larger values of $a/M$ and $g/\left(\sqrt{\frac{3}{2}}M^{2/3}\right)$.

It is instructive to compare the differences between the shadows cast by two different types of black holes, namely a Bardeen black hole and aregular black hole with $\gamma = 2/3$ and $n = 2$. Thus, we plotted the shadows of these two black holes with the same parameter values, as illustrated in Figure 2. Interestingly, we found the silhouette of the shadow cast by the black hole with $\gamma = 2/3$ and $n = 2$ was more deformed than that of the Bardeen black hole, although in general, their sizes and shapes were quite similar. From the insets in Figure 2, one finds that they had a distinct trajectory on the left edge of the circle. Such a discrepancy may be understood as the reflection of their different structures inside the horizons of black holes, where the former has a Minkowski core while the latter has a de Sitter core. In particular, in [39], it was disclosed that for a regular black hole with $\gamma = 2/3$ and $n = 2$, the position with the maximum Kretschmann scalar curvature ran away from the core of the black hole, while for the Bardeen black hole, the position of the maximal Kretschmann scalar curvature was maintained at the center of the hole. In this sense, a regular black hole with $\gamma = 2/3$ and $n = 2$ may become more attractive to photons such that the silhouette of the shadow is more deformed in comparison with that of a Bardeen black hole.

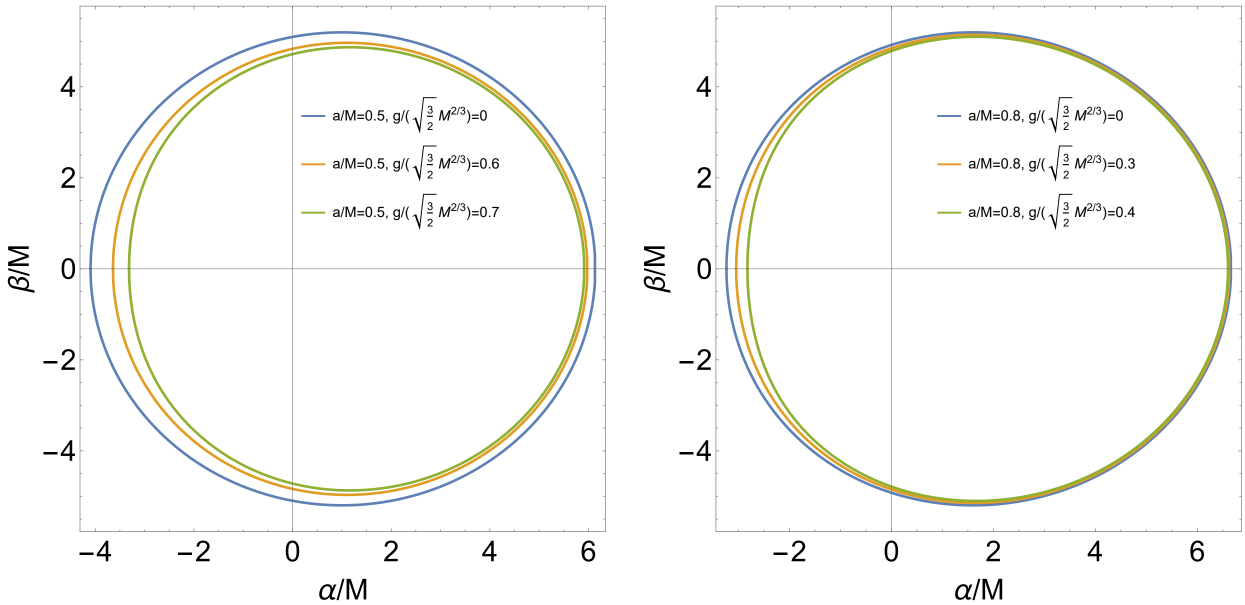


**Figure 1.** The silhouette of the shadow cast by the regular black hole with $\gamma = 2/3$ and $n = 2$ for various values of $g/\left(\sqrt{\frac{3}{2}}M^{2/3}\right)$ with $\theta_0 = \pi/2$. For the left plot, the rotation parameter $a/M$ is fixed at $a/M = 0.5$, while for the right plot, it is fixed at $a/M = 0.8$.

Furthermore, in order to measure the size and deformation of the shadow quantitatively, we introduce two observables to characterize the shadows of black holes, namely the shadow radius $R_s$ and the distortion parameter $\delta_s$ [14], which are given by

$$\begin{aligned} R_s &= \frac{(\alpha_t - \alpha_r)^2 + \beta_t^2}{2(\alpha_t - \alpha_r)}, \\ \delta_s &= \frac{(\tilde{\alpha}_r - \alpha_p)}{R_s}, \end{aligned} \tag{32}$$

where $(\alpha_t, \beta_t)$, $(\alpha_r, 0)$, $(\alpha_p, 0)$ are the coordinates of the shadow vertices at top, right and left edges, respectively, while $(\tilde{\alpha}_r, 0)$ represents the coordinates of the left edges of the reference circle.

The schematic diagram is shown in Figure 3. In Figure 4, we find that the shadow radius $R_s$ monotonically decreased as a function of $g/\left(\sqrt{\frac{3}{2}}M^{2/3}\right)$ for both sorts of regular black holes, while the distortion parameter $\delta_s$ monotonically increased with the increase in the deviation parameter. In particular, we found that for larger values of the deviation parameter, the difference between the two black holes became more pronounced, and the shadow cast by the regular black hole with $\gamma = 2/3$ and $n = 2$ had more distortion than that cast by the Bardeen black hole.

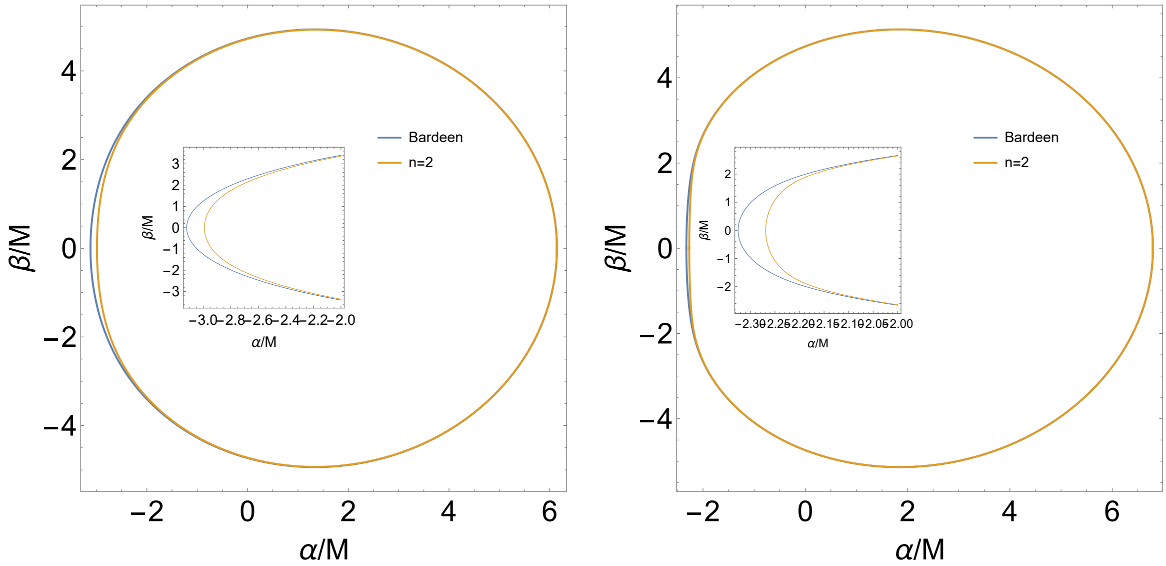


**Figure 2.** The shadows of the black hole with $\gamma = 2/3$ and $n = 2$ and the Bardeen black hole with $\theta_0 = \pi/2$. For both black holes, the parameters were fixed at $a/M = 0.6$ and $g/\left(\sqrt{\frac{3}{2}}M^{2/3}\right) = 0.64$ in the left plot, while they were $a/M = 0.9$ and $g/\left(\sqrt{\frac{3}{2}}M^{2/3}\right) = 0.32$ in the right plot. The insets zoom in on the part near the left edge of the circle.

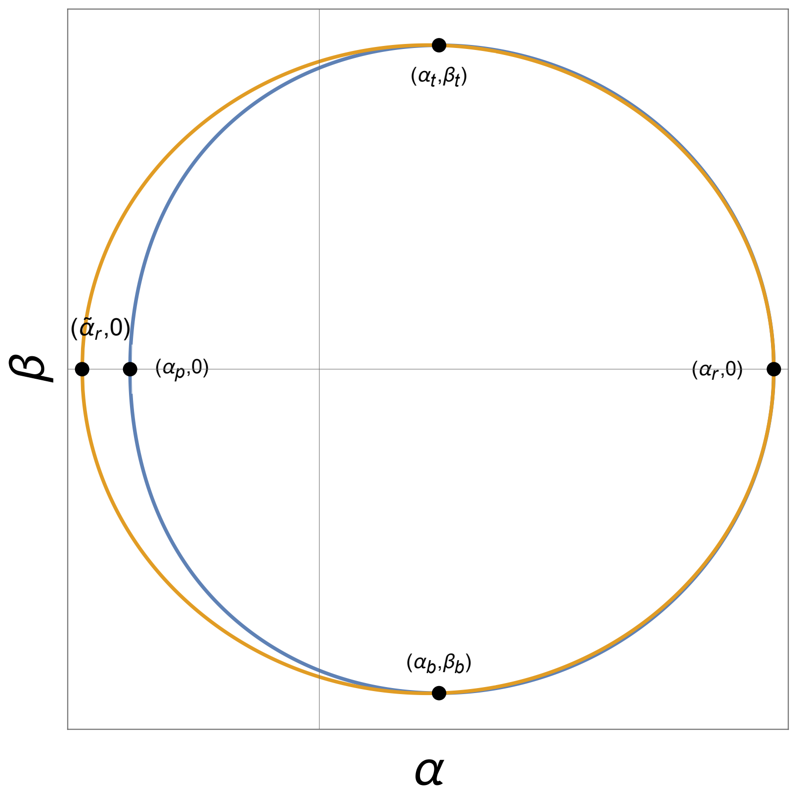


**Figure 3.** The schematic diagram for defining the observables to measure the size and deformation of the shadows.

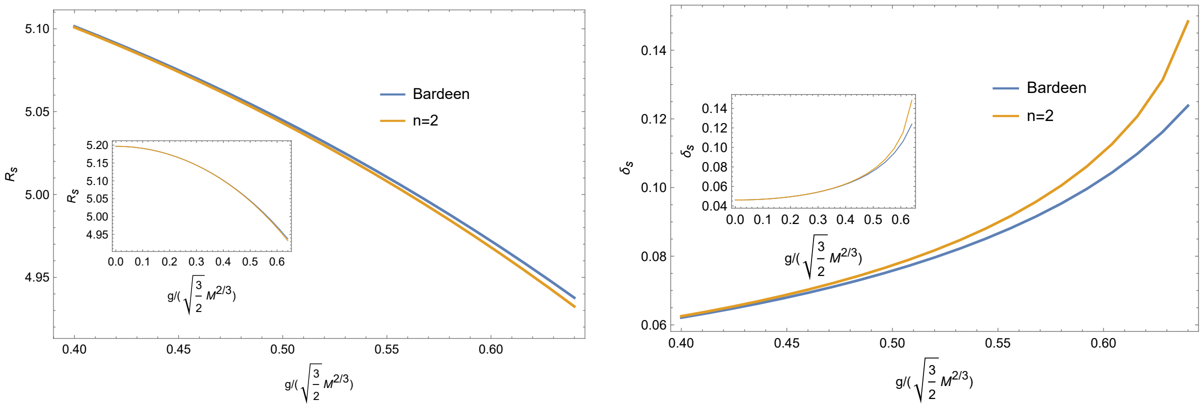


**Figure 4.** The shadow radius $R_s$ as a function of $g/\left(\sqrt{\frac{3}{2}}M^{2/3}\right)$ (**left**). The distorting parameter $\delta_s$ as a function of $g/\left(\sqrt{\frac{3}{2}}M^{2/3}\right)$ (**right**). The rotation parameter $a/M$ is fixed at $a/M = 0.6$, and $\theta_0$ is fixed at $\pi/2$.

Finally, we intend to link our theoretical investigation on the shadows of regular black holes to the observation data detected by the ETH. For the first step, we considered the upper limit of the deviation from circularity for the shadows of black holes. As reported in [1,2], for the supermassive black hole M87* at the center of the galaxy M87*, the upper limit of the deviation from circularity is $\Delta C \lesssim 0.1$ for $\theta_0 = 17\pi/180$ [54,55]. The average radius of the shadow is [18]

$$\bar{R} = \frac{1}{2\pi}\int_0^{2\pi} R(\varphi)d\varphi, \tag{33}$$

with

$$R(\varphi) = \sqrt{(\alpha-\alpha_c)^2 + (\beta-\beta_c)^2}, \;\; \varphi \equiv \tan^{-1}\left(\frac{\beta-\beta_c}{\alpha-\alpha_c}\right), \tag{34}$$

where $\alpha_c = \frac{|\alpha_r+\alpha_p|}{2}$, $\beta_c = \frac{|\beta_t+\beta_b|}{2}$. The deviation from circularity $\Delta C$ is given by [56]

$$\Delta C = \frac{1}{\bar{R}}\sqrt{\frac{1}{2\pi}\int_0^{2\pi}(R(\varphi)-\bar{R})^2 d\varphi}. \tag{35}$$

As shown in Figure 5, we made a contour plot for $\Delta C$ in the $(a, g)$ plane for $\theta_0 = 17\pi/180$. It is obvious that the deviation was much smaller than the upper limit observed by the ETH, indicating that the shadow of the regular black hole with $\gamma = 2/3$ and $n = 2$ is highly compatible with the observation data of the ETH. This implies that the current observation data are not capable of identifying the detected black hole to be an ordinary black hole with singularity or a regular black hole without singularity.

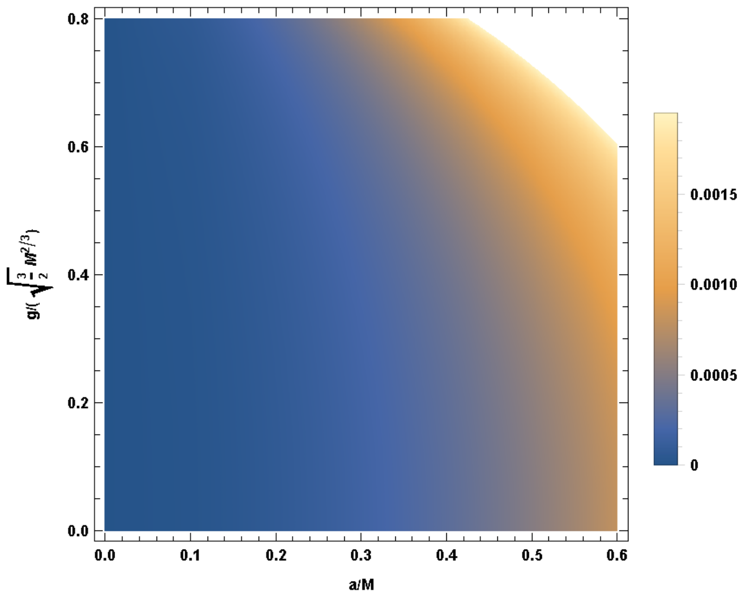


**Figure 5.** The density plot of the deviation from circularity for the regular black hole with $\gamma = 1$ and $n = 2$ in $(a, g)$ plane with $\theta_0 = 17\pi/180$.

## 4. Shadow of the Regular Black Hole with $\gamma = 1$ and $n = 3$

In this section, we study the shadow of the regular black hole with $\gamma = 1$ and $n = 3$ in a parallel way which corresponds to a Hayward black hole at a large scale in the radial direction.

We plotted the silhouettes of the shadows for different values of $g/M^{2/3}$ in Figure 6. Again, we found that with the increase in the values $g/M^{2/3}$, the size of the shadow shrank, while the shape of the shadow became increasingly asymmetrical with respect to the vertical axis.

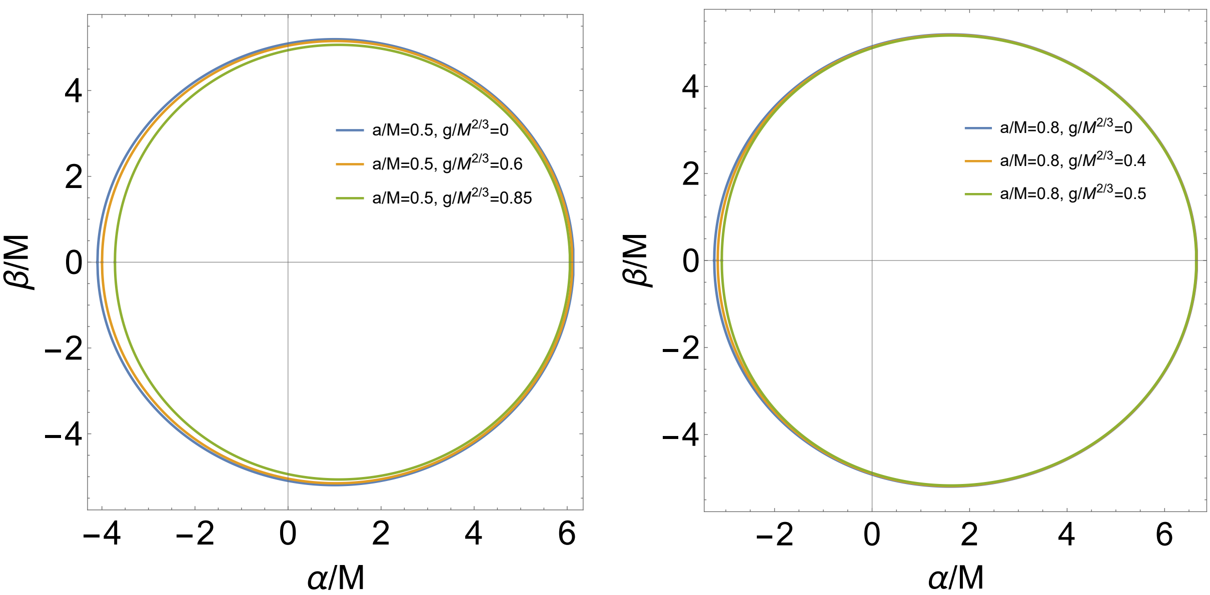


**Figure 6.** The silhouettes of the shadows cast by the regular black hole with $\gamma = 1$ and $n = 3$ for various values of $g/M^{2/3}$ with $\theta_0 = \pi/2$. For the left plot, the rotation parameter $a/M$ is fixed at $a/M = 0.5$, while for the right plot, it is fixed at $a/M = 0.8$.

Next, we compared the differences between the shadow cast by the regular black hole with $\gamma = 1$ and $n = 3$ and that of the Hayward black hole, as shown in Figure 7. Similarly, we found that the size of the shadow cast by the regular black hole with $\gamma = 1$ and $n = 3$

was smaller than that of the Hayward black hole with the same parameter values. In addition, we plotted diagrams for the shadow radius $R_s$ and the distortion parameter $\delta_s$ for these two black holes in Figure 8. Again, we noticed that the difference between these two types of black holes became more significant for larger values of $g/M^{2/3}$. Therefore, based on our above analysis, we intend to conclude that given the same parameter values, the size of the shadow cast by the regular black hole with an asymptotic Minkowski core is always smaller than that of the black hole with an asymptotic de Sitter core, but the deformation of the shadow is greater.

In the end, we also compared the theoretical value of deviation from circularity $\Delta C$ for the black hole with $\gamma = 1$ and $n = 3$ to the results from the ETH, as shown in Figure 9. We found that the shadow of the regular black hole with $\gamma = 1$ and $n = 3$ was highly compatible with the observation data of the ETH $\Delta C \lesssim 0.1$ for $\theta_0 = 17\pi/180$.

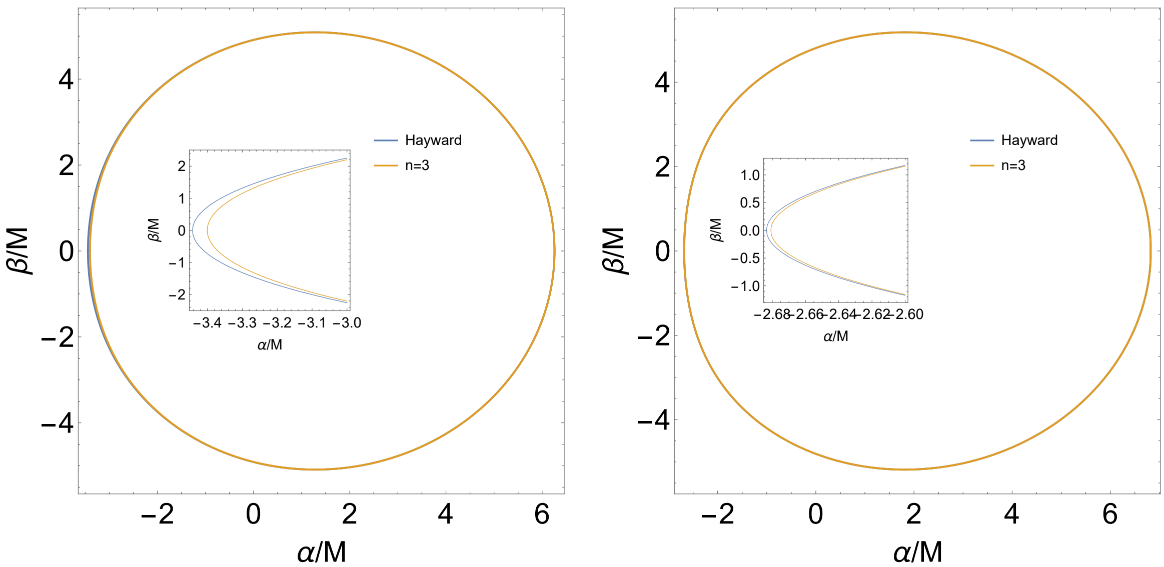


**Figure 7.** The shadows of the black hole with $\gamma = 1$ and $n = 3$ and the Hayward black hole with $\theta_0 = \pi/2$. For both black holes, the parameters were fixed at $a/M = 0.6$ and $g/M^{2/3} = 0.8$ in the left plot and $a/M = 0.9$ and $g/M^{2/3} = 0.41$ in the right plot. The insets zoom in on the part near the left edge of the circle.

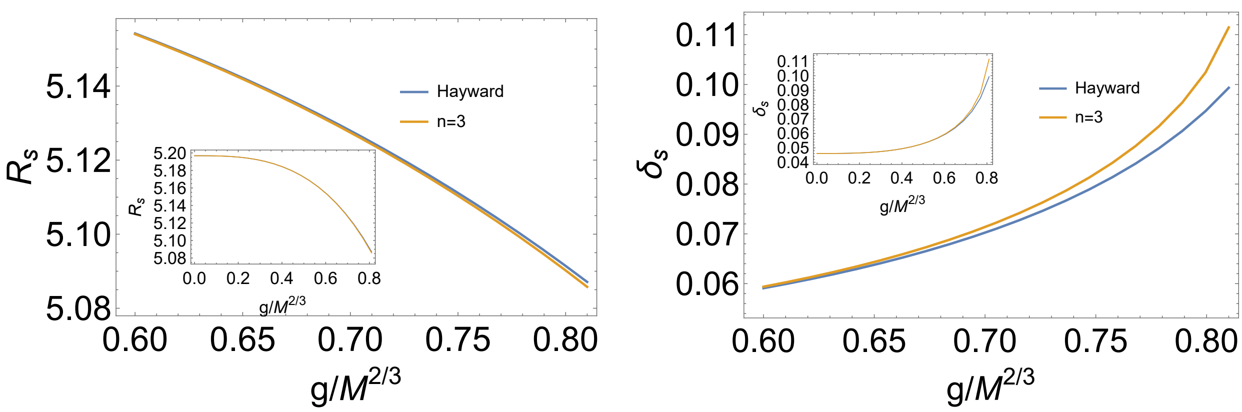


**Figure 8.** The shadow radius $R_s$ as a function of $g/M^{2/3}$ (**left**). The distorting parameter $\delta_s$ as a function of $g/M^{2/3}$ (**right**). The rotation parameter $a/M$ is fixed at $a/M = 0.6$, and $\theta_0$ is fixed at $\pi/2$.

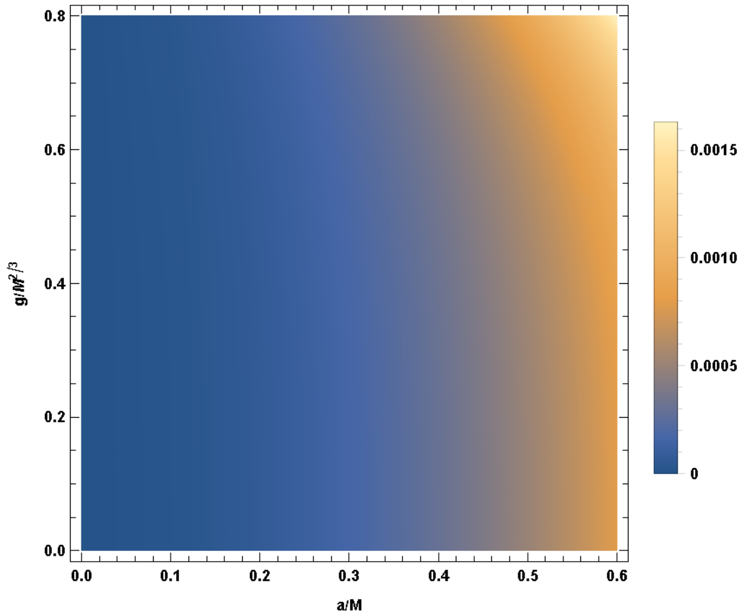


**Figure 9.** The density plot of the deviation from circularity for the regular black hole with $\gamma = 1$ and $n = 3$ in $(a, g)$ plane with $\theta_0 = 17\pi/180$.

## 5. Conclusions and Discussion

In this paper, we investigated the shadows cast by rotating Kerr-like regular black holes with Minkowski cores. We plotted the silhouette of a shadow cast by a regular black hole with $(\gamma = 2/3, n = 2)$ and $(\gamma = 1, n = 3)$, which corresponded to the Bardeen black hole and Hayward black hole at large scales in the radial direction, respectively. It was found that with the increase in the deviation parameter $g$, the left side of the silhouette of the shadow was more inclined toward the vertical axis. Then, the size of the shadow and the shape of the shadow were evaluated by the shadow radius and the distortion parameter. It turned out that with the increase in the deviation parameter $g$, the shadow radius decreased, while the deformation became more and more pronounced. This phenomenon could be understood as follows. The traditional regular black holes can be viewed as solutions of gravity coupled to nonlinear electrodynamics [57–59], and the parameter $g$ in this paper may be viewed as the charge of the nonlinear electromagnetic field. Just as the increase in charge made the size of the black hole horizon smaller, the corresponding size of the shadow shrank, while the shape of the shadow became more deformed [32,45,60]. Furthermore, we compared the shadows for two different types of regular black holes with the same parameter values. In comparison with the regular black holes with de Sitter cores, the size of the shadow was always smaller, and the deformation of the shape became more pronounced as well. One could understand this by comparing the positions of the maximal Kretschmann scalar curvature. As revealed in [39], for regular black holes with Minkowski cores, the position of the maximal Kretschmann scalar curvature moves away from the center of the black hole and is close to the horizon with the increase in the parameter $g$, while for regular black holes with de Sitter cores, the position of the maximal Kretschmann scalar curvature always remains at the center. This may lead to greater attraction of the regular black hole with Minkowski cores to photons. As a result, the silhouette of its shadow is indeed more distorted compared with that of a regular black hole with a de Sitter core. Finally, we also compared the theoretical values of the deviation from circularity $\Delta C$ for two sorts of black holes with the experimental results of the ETH and found that the shadows of regular black holes were highly compatible with the shadows observed by the ETH as well. Therefore, regular black holes are also possible candidates for detected black holes, and further exploration is needed to reveal the nature of black holes observed in astrophysics. Our work provides a theoretical basis for identifying different types of regular black holes once more astronomical black hole images are obtained in the future. Just as discussed in [39], these two different types of regular black holes result from different forms of Newtonian potential, which might imply the different forms of generalized uncertainty relations in the theory of quantum gravity. Thus, we expect that the distinction of regular black holes by astronomical observations would be a great hint for us to look for the effect of quantum gravity. In particular, the exponential form of the Newtonian potential, which gives rise to regular black holes with Minkowski cores [39], could reveal the non-perturbative effects of quantum gravity because in the expansion of weak momentum, it recovers the quadratic form of the momentum, which leads to regular black holes with de Sitter cores [61].

Of course, we may investigate the shadows cast by regular black holes in the presence of plasma, as performed for Bardeen and Hayward black holes, in [30]. It is worth pointing out that what we analyzed in this paper is an integrable system, due to the existence of the Carter constant. It is interesting to consider a non-integrable system surrounding a black hole by breaking the Carter constant [62]. In this case, the trajectory of the light near the black hole may produce chaos, which will provide more information for regular black holes.

**Author Contributions:** The authors contributed equally in the preparation of this article. All authors have read and agreed to the published version of the manuscript.

**Funding:** This work was supported in part by the Natural Science Foundation of China under Grant Nos. 11875053 and 12035016. It was also supported by the Beijing Natural Science Foundation under Grant No. 1222031.

**Institutional Review Board Statement:** Not applicable.

**Informed Consent Statement:** Not applicable.

**Data Availability Statement:** Not applicable.

**Acknowledgments:** We are very grateful to Xin Wu, Xiaomei Kuang and Hong Guo for their helpful discussions.

**Conflicts of Interest:** The authors declare no conflict of interest.

## References

1. The Event Horizon Telescope Collaboration; Akiyama, K.; Alberdi, A.; Alef, W.; Asada, K.; Azulay, R.; Baczko, A.-K.; Ball, D.; Baloković, M.; Barrett, J.; et al. First M87 Event Horizon Telescope Results. I. The Shadow of the Supermassive Black Hole. *Astrophys. J. Lett.* **2019**, *875*, L1. [CrossRef]
2. The Event Horizon Telescope Collaboration; Akiyama, K.; Alberdi, A.; Alef, W.; Asada, K.; Azulay, R.; Baczko, A.-K.; Ball, D.; Baloković, M.; Barrett, J.; et al. First M87 Event Horizon Telescope Results. IV. Imaging the Central Supermassive Black Hole. *Astrophys. J. Lett.* **2019**, *875*, L4. [CrossRef]
3. Akiyama, K.; Alberdi, A.; Alef, W.; Algaba, J.C.; Anantua, R.; Asada, K.; Azulay, R.; Bach, U.; Baczko, A.K.; Ball, D.; et al. First Sagittarius A* Event Horizon Telescope Results. I. The Shadow of the Supermassive Black Hole in the Center of the Milky Way. *Astrophys. J. Lett.* **2022**, *930*, L12.
4. Akiyama, K.; Alberdi, A.; Alef, W.; Algaba, J.C.; Anantua, R.; Asada, K.; Azulay, R.; Bach, U.; Baczko, A.K.; Ball, D.; et al. First Sagittarius A* Event Horizon Telescope Results. III. Imaging of the Galactic Center Supermassive Black Hole. *Astrophys. J. Lett.* **2022**, *930*, L14.
5. Synge, J.L. The Escape of Photons from Gravitationally Intense Stars. *Mon. Not. R. Astron. Soc.* **1966**, *131*, 463–466. [CrossRef]
6. Luminet, J.P. Image of a spherical black hole with thin accretion disk. *Astron. Astrophys.* **1979**, *75*, 228–235.
7. Bardeen, J.M. *Black Holes (Les Astres Occlus)*; DeWitt, C., DeWitt, B.S., Eds.; Gordon and Breach: New York, NY, USA, 1973; pp. 215–239.
8. Chandrasekhar, S. *The Mathematical Theory of Black Holes*; Oxford University Press: New York, NY, USA, 1992.
9. Cunha, P.V.P.; Herdeiro, C.A.R. Shadows and strong gravitational lensing: A brief review. *Gen. Relativ. Gravit.* **2018**, *50*, 1–27. [CrossRef]
10. Hu, Z.; Zhong, Z.; Li, P.-C.; Guo, M.; Chen, B. QED effect on a black hole shadow. *Phys. Rev. D* **2021**, *103*, 044057. [CrossRef]
11. Ling, R.; Guo, H.; Liu, H.; Kuang, X.-M.; Wang, B. Shadow and near-horizon characteristics of the acoustic charged black hole in curved spacetime. *Phys. Rev. D* **2021**, *104*, 104003. [CrossRef]
12. Perlick, V.; Tsupko, O.Y. Calculating black hole shadows: Review of analytical studies. *Phys. Rep.* **2021**, *947*, 1–39. [CrossRef]
13. Takahashi, R. Black Hole Shadows of Charged Spinning Black Holes: Fig. 1. *Publ. Astron. Soc. Jpn.* **2005**, *57*, 273–277. [CrossRef]

14. Hioki, K.; Maeda, K.-I. Measurement of the Kerr spin parameter by observation of a compact object's shadow. *Phys. Rev. D* **2009**, *80*, 024042. [CrossRef]
15. Tsupko, O.Y. Analytical calculation of black hole spin using deformation of the shadow. *Phys. Rev. D* **2017**, *95*, 104058. [CrossRef]
16. Bambi, C.; Freese, K.; Vagnozzi, S.; Visinelli, L. Testing the rotational nature of the supermassive object M87* from the circularity and size of its first image. *Phys. Rev. D* **2019**, *100*, 044057. [CrossRef]
17. Badía, J.; Eiroa, E.F. Shadow of axisymmetric, stationary, and asymptotically flat black holes in the presence of plasma. *Phys. Rev. D* **2021**, *104*, 084055. [CrossRef]
18. Johannsen, T.; Psaltis, D. Testing the no-hair theorem with observations in the electromagnetic spectrum. II. Black hole images. *Astrophys. J. Lett.* **2010**, *718*, 446–454. [CrossRef]
19. Wei, S.-W.; Liu, Y.-X. Observing the shadow of Einstein-Maxwell-Dilaton-Axion black hole. *J. Cosmol. Astropart. Phys.* **2013**, *2013*, 063. [CrossRef]
20. Amir, M.; Ghosh, S.G. Shapes of rotating nonsingular black hole shadows. *Phys. Rev. D* **2016**, *94*, 024054. [CrossRef]
21. Xu, Z.; Hou, X.; Wang, J. Possibility of identifying matter around rotating black hole with black hole shadow. *J. Cosmol. Astropart. Phys.* **2018**, *2018*, 046. [CrossRef]
22. Yan, S.-F.; Li, C.; Xue, L.; Ren, X.; Cai, Y.-F.; Easson, D.A.; Yuan, Y.-F.; Zhao, H. Testing the equivalence principle via the shadow of black holes. *Phys. Rev. Res.* **2020**, *2*, 023164. [CrossRef]
23. Guo, M.; Li, P.-C. Innermost stable circular orbit and shadow of the 4D Einstein–Gauss–Bonnet black hole. *Eur. Phys. J. C* **2020**, *80*, 1–8. [CrossRef]
24. Liu, C.; Zhu, T.; Wu, Q.; Jusufi, K.; Jamil, M.; Azreg-Aïnou, M.; Wang, A. Shadow and quasinormal modes of a rotating loop quantum black hole. *Phys. Rev. D* **2020**, *101*, 084001. [CrossRef]
25. Badía, J.; Eiroa, E.F. Influence of an anisotropic matter field on the shadow of a rotating black hole. *Phys. Rev. D* **2020**, *102*, 024066. [CrossRef]
26. Vagnozzi, S.; Visinelli, L. Hunting for extra dimensions in the shadow of M87*. *Phys. Rev. D* **2019**, *100*, 024020. [CrossRef]
27. Khodadi, M.; Allahyari, A.; Vagnozzi, S.; Mota, D.F. Black holes with scalar hair in light of the Event Horizon Telescope. *J. Cosmol. Astropart. Phys.* **2020**, *2020*, 026. [CrossRef]
28. Vagnozzi, S.; Roy, R.; Tsai, Y.D.; Visinelli, L. Horizon-scale tests of gravity theories and fundamental physics from the Event Horizon Telescope image of Sagittarius $A^*$. *arXiv* **2022**, arXiv:2205.07787.
29. Lee, B.-H.; Lee, W.; Myung, Y.S. Shadow cast by a rotating black hole with anisotropic matter. *Phys. Rev. D* **2021**, *103*, 064026. [CrossRef]
30. Abdujabbarov, A.; Amir, M.; Ahmedov, B.; Ghosh, S.G. Shadow of rotating regular black holes. *Phys. Rev. D* **2016**, *93*, 104004. [CrossRef]
31. Tsukamoto, N. Black hole shadow in an asymptotically flat, stationary, and axisymmetric spacetime: The Kerr-Newman and rotating regular black holes. *Phys. Rev. D* **2018**, *97*, 064021. [CrossRef]
32. Kumar, R.; Ghosh, S.G.; Wang, A. Shadow cast and deflection of light by charged rotating regular black holes. *Phys. Rev. D* **2019**, *100*, 124024. [CrossRef]
33. Kumar, A.; Baboolal, D.; Ghosh, S.G. Nonsingular Black Holes in 4D Einstein–Gauss–Bonnet Gravity. *Universe* **2022**, *8*, 244. [CrossRef]
34. Bardeen, J.M. *Proceedings of the International Conference GR5*; Tbilisi University Press: Tbilisi, Georgia, 1968; pp. 174–180.
35. Hayward, S.A. Formation and Evaporation of Nonsingular Black Holes. *Phys. Rev. Lett.* **2006**, *96*, 031103. [CrossRef]
36. Frolov, V.P. Information loss problem and a 'black hole' model with a closed apparent horizon. *J. High Energy Phys.* **2014**, *2014*, 49. [CrossRef]
37. Ansoldi, S. Spherical black holes with regular center: A Review of existing models including a recent realization with Gaussian sources. *arXiv* **2008**, arXiv:0802.0330.
38. Xiang, L.; Ling, Y.; Shen, Y.G. Singularities and the Finale of Black Hole Evaporation. *Int. J. Mod. Phys. D* **2013**, *22*, 1342016. [CrossRef]
39. Ling, Y.; Wu, M.H. Regular black holes with sub-Planckian curvature. *arXiv* **2021**, arXiv:2109.05974.
40. Ling, Y.; Wu, M.-H. Modified regular black holes with time delay and 1-loop quantum correction *. *Chin. Phys. C* **2022**, *46*, 025102. [CrossRef]
41. Bargueño, P. Some global, analytical, and topological properties of regular black holes. *Phys. Rev. D* **2020**, *102*, 104028. [CrossRef]
42. Melgarejo, G.; Contreras, E.; Bargueño, P. Regular black holes with exotic topologies. *Phys. Dark Universe* **2020**, *30*, 100709. [CrossRef]
43. Berry, T.; Lobo, F.S.N.; Simpson, A.; Visser, M. Thin-shell traversable wormhole crafted from a regular black hole with asymptotically Minkowski core. *Phys. Rev. D* **2020**, *102*, 064054. [CrossRef]
44. Simpson, A.; Visser, M. The eye of the storm: A regular Kerr black hole. *J. Cosmol. Astropart. Phys.* **2022**, *2022*, 011. [CrossRef]
45. Banerjee, I.; Sau, S.; SenGupta, S. Signatures of regular black holes from the shadow of Sgr A* and M87*. *J. Cosmol. Astropart. Phys.* **2022**, *2022*, 066. [CrossRef]
46. Ayón-Beato, E.; García, A. Regular Black Hole in General Relativity Coupled to Nonlinear Electrodynamics. *Phys. Rev. Lett.* **1998**, *80*, 5056–5059. [CrossRef]
47. Newman, E.T.; Janis, A.I. Note on the Kerr spinning-particle metric. *J. Math. Phys.* **1965**, *6*, 915–917. [CrossRef]

48. Azreg-Aïnou, M. Generating rotating regular black hole solutions without complexification. *Phys. Rev. D* **2014**, *90*, 064041. [CrossRef]
49. Azreg-Aïnou, M. From static to rotating to conformal static solutions: Rotating imperfect fluid wormholes with(out) electric or magnetic field. *Eur. Phys. J. C* **2014**, *74*, 1–11. [CrossRef]
50. Wu, M.H.; Guo, H.; Kuang, X.M. Shadow Cast of Rotating Charged Black Hole with Scalar Q-Hair. *Symmetry* **2022**, *14*, 2237. [CrossRef]
51. Azreg-Aïnou, M. Regular and conformal regular cores for static and rotating solutions. *Phys. Lett. B* **2014**, *730*, 95–98. [CrossRef]
52. Toshmatov, B.; Ahmedov, B.; Abdujabbarov, A.; Stuchlík, Z. Rotating regular black hole solution. *Phys. Rev. D* **2014**, *89*, 104017. [CrossRef]
53. Ghosh, S.G. A nonsingular rotating black hole. *Eur. Phys. J. C* **2015**, *75*, 1–7. [CrossRef]
54. Walker, R.C.; Hardee, P.E.; Davies, F.B.; Ly, C.; Junor, W. The Structure and Dynamics of the Subparsec Jet in M87 Based on 50 VLBA Observations over 17 Years at 43 GHz. *Astrophys. J. Lett.* **2018**, *855*, 128. [CrossRef]
55. Kuang, X.-M.; Tang, Z.-Y.; Wang, B.; Wang, A. Constraining a modified gravity theory in strong gravitational lensing and black hole shadow observations. *Phys. Rev. D* **2022**, *106*, 064012. [CrossRef]
56. Afrin, M.; Kumar, R.; Ghosh, S.G. Parameter estimation of hairy Kerr black holes from its shadow and constraints from M87*. *Mon. Not. R. Astron. Soc.* **2021**, *504*, 5927–5940. [CrossRef]
57. Ayón-Beato, E.; Garcia, A. Non-Singular Charged Black Hole Solution for Non-Linear Source. *Gen. Relativ. Gravit.* **1999**, *31*, 629–633. [CrossRef]
58. Ayon-Beato, E.; Garcia, A. New regular black hole solution from nonlinear electrodynamics. *Phys. Lett. B* **1999**, *464*, 25–29. [CrossRef]
59. Ma, M.-S. Magnetically charged regular black hole in a model of nonlinear electrodynamics. *Ann. Phys.* **2015**, *362*, 529–537. [CrossRef]
60. Jafarzade, K.; Zangeneh, M.K.; Lobo, F.S. Shadow, deflection angle and quasinormal modes of Born-Infeld charged black holes. *J. Cosmol. Astropart. Phys.* **2021**, *2021*, 008. [CrossRef]
61. Xiang, L.; Ling, Y.; Shen, Y.-G.; Liu, C.-Z.; He, H.-S.; Xu, L.-F. Generalized uncertainty principles, effective Newton constant and the regular black hole. *Ann. Phys.* **2018**, *396*, 334–350. [CrossRef]
62. Wang, Y.; Sun, W.; Liu, F.; Wu, X. Construction of Explicit Symplectic Integrators in General Relativity. I. Schwarzschild Black Holes. *Astrophys. J. Lett.* **2021**, *907*, 66. [CrossRef]